

## Microstructural Dependence of Strain Rate Sensitivity in Thermomechanically Processed $\text{Al}_{0.1}\text{CoCrFeNi}$ High Entropy Alloy

Sindhura Gangireddy<sup>a</sup>, Liu Kaimiao<sup>b</sup>, Bharat Gwalani<sup>a</sup>, Rajiv Mishra<sup>a</sup>

<sup>a</sup>AMMPI, University of North Texas, Denton, TX 76207

<sup>b</sup>Materials Science and Engineering, University of North Texas, Denton, TX 76207

### Abstract

$\text{Al}_{0.1}\text{CoCrFeNi}$  is a single-phase *FCC* high entropy alloy (HEA) that promises remarkable work-hardening due to its low stacking fault energy (SFE) resulting in suppression of cross-slip and dynamic recovery. The cast material of low yield strength was cold-worked to enhance strength; and then subjected to recovery and recrystallization treatments to improve ductility. Mechanical responses from standard tensile testing at quasi-static strain rate of  $10^{-3} \text{ s}^{-1}$  were coupled with dynamic deformation from split-Hopkinson pressure bar (SHPB) testing at  $10^3 \text{ s}^{-1}$  to study strain rate sensitivity (SRS) and its microstructural dependence in various conditions generated by thermomechanical processing. While dynamic work-hardening remained high in all microstructural conditions, SRS was highly sensitive to the nature of obstacles in each condition. The cast condition showed a moderate SRS of 0.017, but introduction of dislocation tangles and large deformation twins with cold work rendered a sharp drop in SRS to  $\sim 0$ . As the density of these defects is reduced during low-temperature annealing treatments, the recovered microstructures showed SRS recuperating back to original SRS level of 0.017. Higher temperature treatments resulted in partial recrystallization and lower  $\text{SRS} < 0.008$  due to additional strength contribution from grain refinement in the recrystallized portions and remnant cold work in unrecrystallized portions. Dynamic work-hardening remained very high at  $\sim 1600 \text{ MPa}$  in all conditions from a combination of dynamic recovery suppression and intense twinning that is inherent to the HEA due to its low SFE.

### Keywords:

High entropy alloy;  $\text{Al}_x\text{CoCrFeNi}$ ; strain rate sensitivity; dynamic mechanical behavior; thermomechanical processing.

### Introduction

A new paradigm of metallic alloy development by stabilizing simple microstructures with multiple elements in equimolar proportions has emerged. This class of materials known as high entropy alloys (HEAs) was proposed to have significant multi-element effects as compared with conventional alloys. The four core effects of high entropy, sluggish diffusion, lattice distortion and cocktail effects have been studied extensively [1-4]. They offer potential for promising properties such as high strength combined with good ductility from simple crystal structures.  $\text{Al}_x\text{CoCrFeNi}$  is prominent among the several alloy systems identified on the basis of this design strategy. It changes from *FCC* to *BCC* structure with increasing aluminum content and demonstrates a wide spectrum of mechanical behavior [5-8].  $\text{Al}_{0.1}\text{CoCrFeNi}$  ( $x=0.1$ ) is a single-phase *FCC* HEA which is stable even at high temperatures [9]. Strengthening from multi-element solid solution, which is controlled by thermally activated deformation, can offer higher strain rate sensitivity (SRS) in this HEA than conventional FCC metals.  $\text{Al}_{0.1}\text{CoCrFeNi}$  ( $x=0.1$ ) is

also expected to have a very low stacking fault energy, SFE <30 mJ/mm<sup>2</sup> [10]. In a similar FCC HEA, CoCrFeNiMn, of low SFE dissociation of several dislocations into 1/6 <112> Shockley partials was reported by F.Otto et al. [11]. With such separation between dislocation partials, cross-slip/dislocation climb would be inhibited and dynamic recovery processes would be suppressed [12]. As reorganization of dislocations, and hence lattice relaxation, is hindered, we can anticipate high work-hardening rates and increased twinning propensity. Deformation twinning was reported to be the main mechanism dominating plasticity in cast and recrystallized conditions of Al<sub>0.1</sub>CoCrFeNi by Wu et al. [13]. Slip and twinning were discovered to be parallel processes in CoCrFeMnNi by Moon et al. [14] at 77k in 10<sup>-3</sup> s<sup>-1</sup> - 10<sup>-2</sup> s<sup>-1</sup> strain rate range, conditions akin to dynamic regime at room temperature. Due to these multiple deformation mechanisms, understanding strain rate sensitivity in HEAs becomes complicated than the well-studied conventional FCC or BCC alloys [15, 16]. High work hardening rates also imply that strength gains could be substantial from cold working this low strength alloy, Al<sub>0.1</sub>CoCrFeNi has been reported to have yield strength (YS) of 150-200 MPa [13, 17, 9]. Subjecting this HEA to thermomechanical processing routes would introduce additional strengthening from strain hardening and grain refinement, which are athermal barriers to deformation. Hence strain rate sensitivity (SRS), a microstructure-sensitive parameter, would be expected to vary significantly in these processed conditions. In this study, we investigated the effect of two rolling conditions and four different annealing treatments, of which two were in the recovery regime and the other two in the recrystallization regime. Theoretical and experimental studies on the strain-rate effect of different FCC metals have shown that strain rate sensitivity remains steady in 10<sup>-3</sup> s<sup>-1</sup> - 10<sup>3</sup> s<sup>-1</sup> strain rate range, after which a transition to sharper increase in flow stresses is observed [16, 17, 18]. So it is a common practice to couple mechanical data from wide strain rate regimes to derive the strain rate sensitivity parameters [12, 19, 20]. Following this method, in this study quasi-static response at 10<sup>-3</sup> s<sup>-1</sup> from standard tensile testing and dynamic mechanical response at 10<sup>3</sup> s<sup>-1</sup> from split-Hopkinson pressure bar (SHPB) technique [21] are coupled to study strain rate sensitivity and dynamic work hardening in these heat-treated conditions.

### Experimental Procedure

Plates of Al<sub>0.1</sub>CoCrFeNi single-phase HEA were rolled unidirectionally at room temperature for thickness reductions of 20% and 40%. The 40% cold-worked plates were subjected to annealing treatments. As the melting point of this alloy is expected to be 1655-1690 K [5], the treatment temperatures for recovery were done at low temperatures of 550°C/24h and 620°C/50h, and the two treatments for recrystallization were performed at higher temperatures of 700°C/5h and 800°C/1h. The samples were placed inside pre-heated furnaces and then cooled by water quenching after specified hold time, to eliminate microstructural evolution during heating and cooling ramps. The heat-treated microstructures were studied using scanning electron microscope (SEM) and electron back-scatter diffraction (EBSD). Tensile samples were cut from the plates, perpendicular to the rolling direction, and tested at 10<sup>-3</sup> s<sup>-1</sup> strain rate to obtain quasi-static mechanical properties. Cylindrical samples cut from these same plates, with their

axis perpendicular to the rolling direction, were compressed dynamically using SHPB at  $10^3$  s $^{-1}$  strain rate.

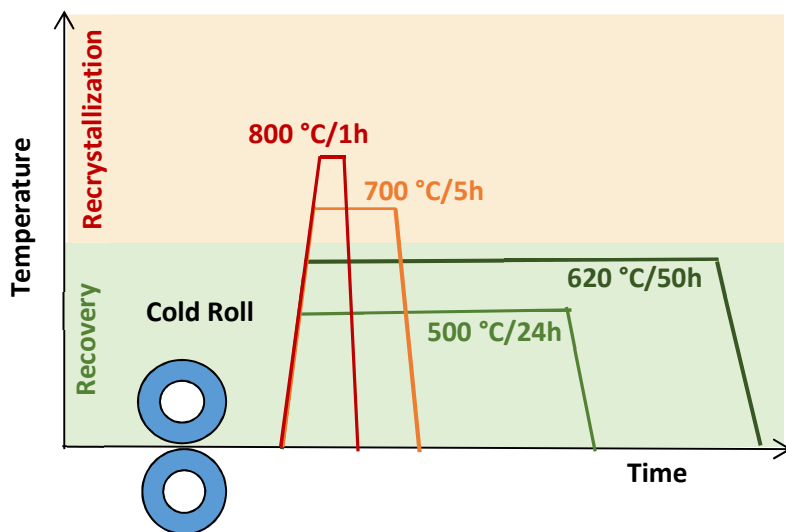


**Figure 1.** Schematic of thermomechanical processing treatments applied to selected specimens of cold-rolled  $\text{Al}_{0.1}\text{CoCrFeNi}$ .

## Results

### Microstructures

The microstructure of the as-cast and 40% cold rolled (40CR) material are presented in Figure 2. The cast material was composed of large equi-axed grains (SEM image in Figure 2 (a)), while the rolled material showed elongated grains with deformation twins of exceptionally large size, several 100  $\mu\text{m}$  in length, as seen from the EBSD image in Figure 2(b).

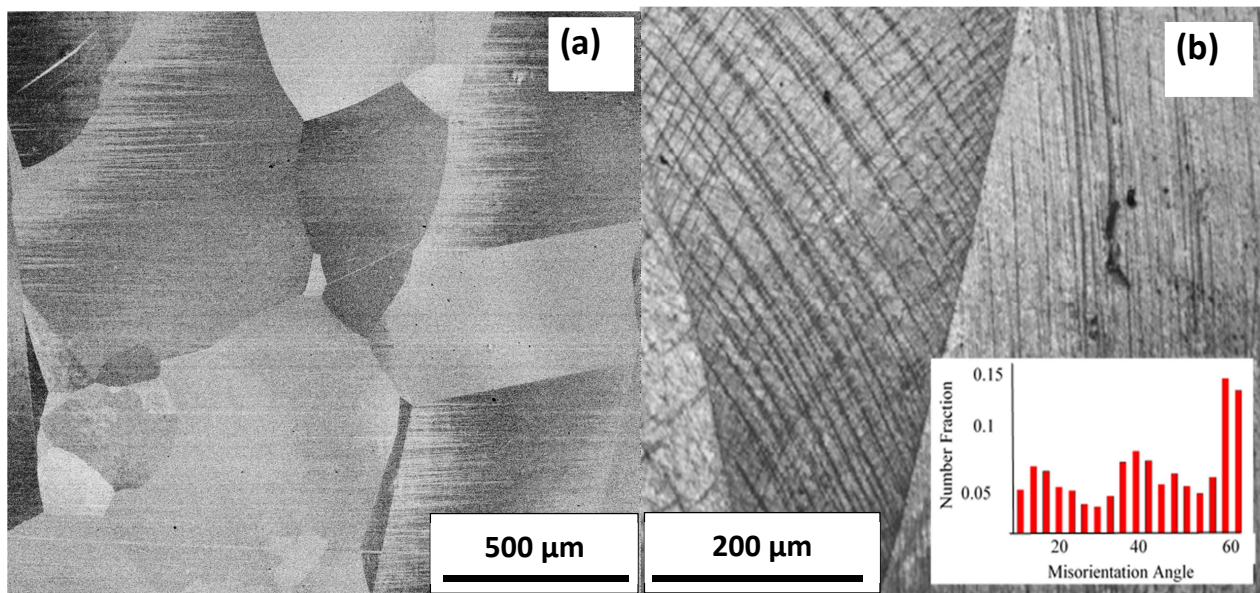


**Figure 2:** (a) SEM image of the cast material (b) IQ-EBSD of 40% rolled (40CR) material showing families of large deformation twins. Inset shows spike in the fraction of 60°/twin fault planes.

The microstructures of the 40% rolled material after the two recovery treatments are shown in Figure 3. The 550°C/24h treatment did not fully recover deformation twins. While not so clearly noticeable as in the as-rolled condition, they were nevertheless detected through misorientation line profiling, as highlighted by Line 1 scan. The microstructure also showed small contrast variations within the grain, indicating bands of deformation, which can form when one portion of the grain undergoes more strain and rotates the grain slightly, without actually forming a grain boundary. These features become more pronounced after higher temperature annealing. Microstructure after 620°C/50h treatment shows well-formed bands (pink bands in the ochre grain in Figure 3) that are very long and ribbon-like, of ~100 µm width, showing about 30° misorientation with respect to the base grain with fuzzy boundaries. These deformation bands were also arrayed by twins (green slivers within the largest pink band), detected by the 60° misorientation of their  $\Sigma 3$  boundaries in the traversing Line 3 profiling.

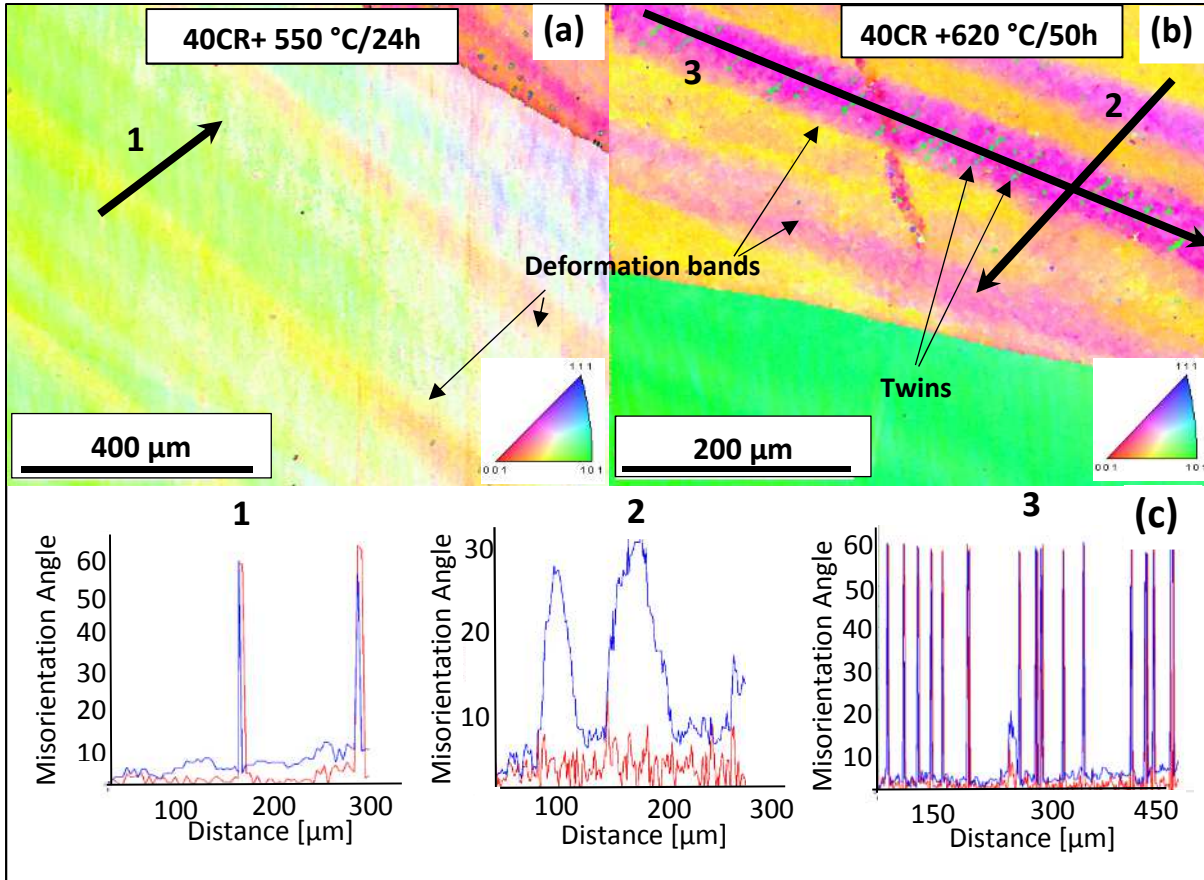
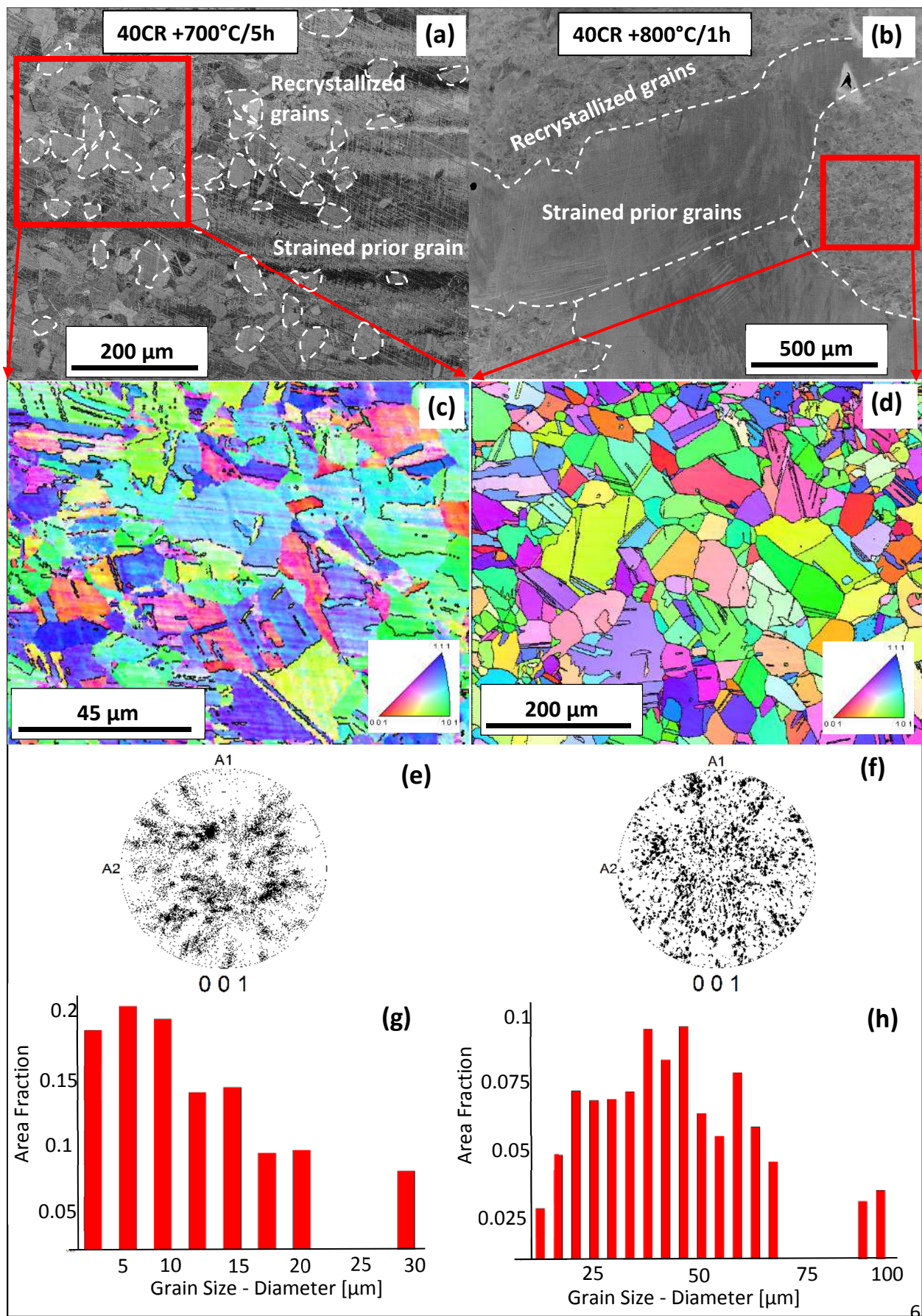


**Figure 3** (a) Microstructures of the 40% rolled material after recovery treatments of 550°C/24h and (b) 620°C/50h in IPF maps. (c) Misorientation profiling on 3 highlighted lines: Line 1 shows two deformation twins in 550°C/24h condition. Lines 2 and 3 in 620°C/50h condition show deformation bands and annealing twins, respectively.

The second set of two heat treatments, intended for recrystallization study, generated very interesting microstructures. Both the 700°C/5h and 800°C/1h treatments resulted in partial/incomplete recrystallization creating heterogeneous microstructures, as summarized in Figure 4. Low magnification SEM images in Figures 4(a) and 4(b) are used to capture the larger scale microstructures, both of which were composed of prior-strained grains and smaller recrystallized grains. However, there were several disparities between these two microstructures:

- The newly formed fine grains were dispersed in the 700°C/5h condition, appearing scattered across the prior grains as seen from Figure 4(a) which highlights some of the recrystallized fine grains. But in the 800°C/1h condition, the recrystallized regions were tightly packed and from Figure 4(b) which highlights the grain boundaries of prior grains, it is clear that each prior grain was either fully recrystallized or remained completely untransformed.
- The recrystallized grains from the lower temperature treatment of 700°C/5h had contrast variations within them indicating intragranular cold work storage, whereas they were fully equi-axed from 800°C/1h treatment.
- The recrystallized grains from 800°C/1h were also significantly larger than those from 700°C/5h. The grain size distribution from the EBSD images shows the 700°C/5h grains were ~5 µm in diameter, while the 800°C/1h grains were ~ 50 µm in size (Figures 4(g) and 4(h)). This suggests that grain growth occurred at 800°C in those regions that had recrystallization.

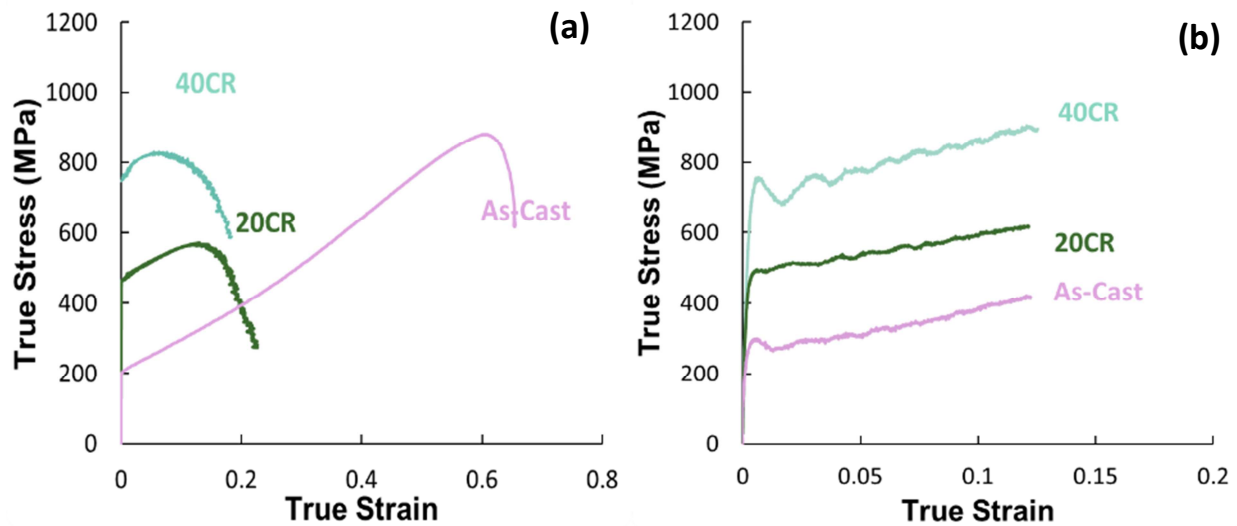
Together, the three differences cited above infer that during 700°C/5h the formation of new grains occurred by dislocation rearrangement and annihilation leading to high angle grain boundary formation, whereas nucleation and grain boundary sweep occurred at 800°C/1h. So 800°C/1h is a true recrystallization treatment for this Al<sub>0.1</sub>CoCrFeNi alloy and is sufficient to cause full recrystallization, provided the prior grains had sufficient strain energy. Wu et al [13] observed full recrystallization in 60% cold rolled Al<sub>0.1</sub>CoCrFeNi HEA with the same 800°C/1h annealing conditions. In our material with 40% cold work, there must have been strain inhomogeneity as a result of which not all grains had enough strain to trigger recrystallization, leading to an overall partially recrystallized microstructure.



**Figure 4.** Microstructures of the 40% rolled material after annealing treatments of 700°C/5h, on left, and 800°C/1h, on right. (a) (b) SEM micrographs, (c) (d) IPF maps from EBSD, (e) (f) Pole figures showing texture, and (g) (h) Grain size distribution from recrystallized region.

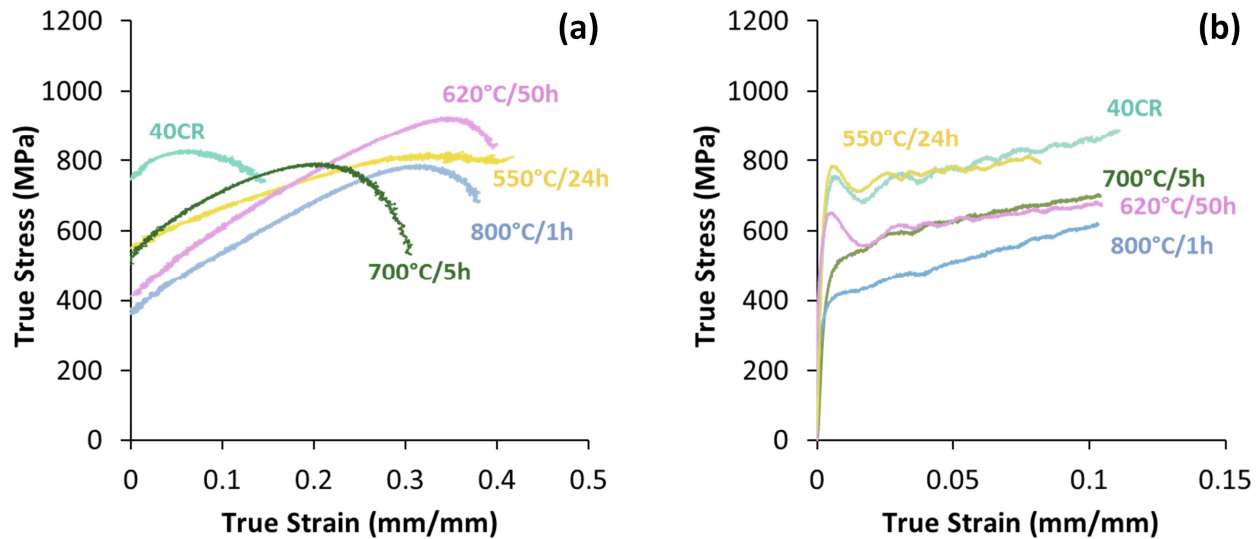
### Mechanical testing

The stress-strain curves from quasi-static tensile testing and dynamic Split-Hopkinson Pressure Bar (SHPB) compression of the pure-rolled materials are compared to the cast condition (Figure 5). The low strain rate (LSR) / quasi-static data show the as-cast material to have a low yield strength of  $YS = \sim 200$  MPa and a ductility of over 60%, similar to that reported in literature [22]. Strength enhancement and ductility deterioration occurred upon cold-rolling. At 20%, strength improved to a  $YS$  of 465 MPa in 20CR, but ductility dropped sharply to 12% uniform elongation. So there was a drop in UTS as well as toughness in the 20CR sample. With cold rolling to 40% (40CR) strength continued to improve ( $YS = 750$  MPa), with ductility dropping further to 6% uniform elongation. But due to higher  $YS$ , the UTS recuperated back to 824 MPa (comparable to as-cast condition) while the toughness increases moderately from 20CR. Pouraliakbar et al have made similar observations in single direct rolled Al-Mn-Si alloy [23, 24]. Hou et al. [25] also have reported that cold working  $Al_{0.25}CoCrFeNi$ , another HEA from the same family with single phase FCC structure, resulted in enormous strength gains with 90% rolled material showing a yield strength 10.9 times higher than its as-cast counterpart. This outstanding cold work strengthening seems peculiar to this family of HEAs and attributed to their low SFE which enhances twinning and hence strain hardening. The dynamic SHPB/HSR performance of these cast and rolled conditions, shown in Figure 5(b), also follow a similar trend. To improve ductility, heat treatments from Figure 1 were conducted on 40% rolled material.



**Figure 5.** True stress-true strain curves of the as-cast and rolled materials with thickness reductions of 20% (20CR) and 40% (40CR): (a) quasi-static tensile testing and (b) SHPB compression.

The mechanical responses of the heat treated conditions are compared to the rolled condition (40CR) in Figure 6. All the treatments improved ductility significantly, bringing uniform elongation to above 20% strain. 550°C/24h treatment shows the highest strength, while 620°C/50h treatment shows highest work hardening rate and resulting in highest UTS, as seen from quasi-static properties in Figure 6(a). From the dynamic response depicted in Figure 6(b), it can be quickly perceived that the trends are different at high strain rate (HSR) regime. The most obvious example is 550°C/24h which has lower strength than pure rolled 40CR in quasi-static regime but shows comparable flow stresses to 40CR in the dynamic regime. This indicates that the strain rate sensitivity is changing significantly across the different annealed conditions. A summary of the quasi-static mechanical properties of these heat treated conditions is presented in Table 1.



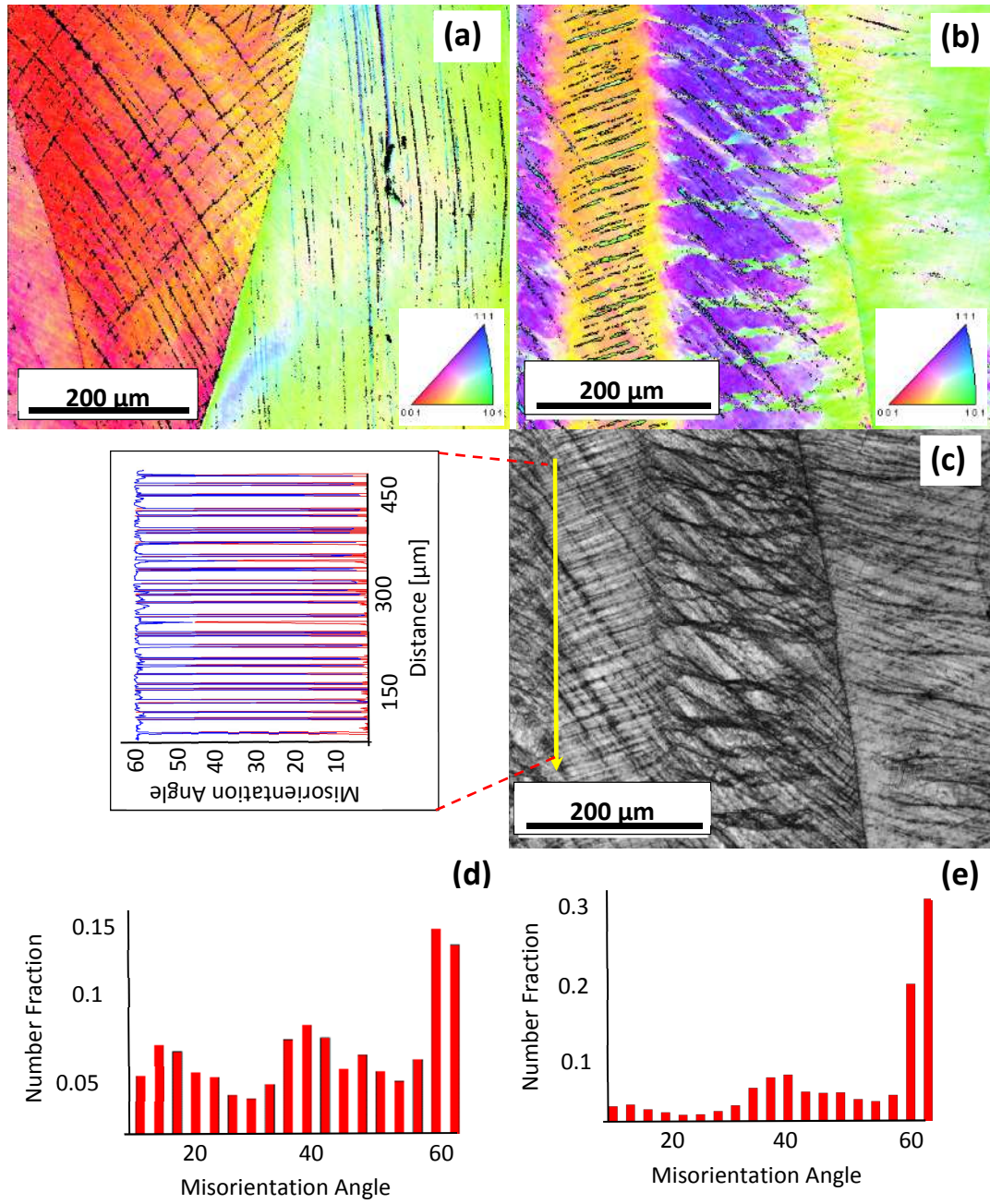
**Figure 6.** True stress-true strain curves of the heat treated conditions compared with the 40% rolled condition in: (a) quasi-static tensile testing and (b) SHPB compression

Table 1: Mechanical properties of the various thermomechanically processed conditions.

	YS (MPa)	UTS (MPa)	Ductility (% failure strain)	Toughness (J/cm <sup>3</sup> )
As-cast	175	880	64%	364
20% CR	464	563	23%	112
40% CR	749	824	14%	148
40%CR+550°C/24h (Recovery)	552	802	42%	285
40%CR+620°C/50h (Recovery)	412	892	40%	268
40%CR+700°C/5h (Partial Recrystallization)	520	779	31%	231
40%CR+800°C/1h (Partial Recrystallization)	360	790	39%	241

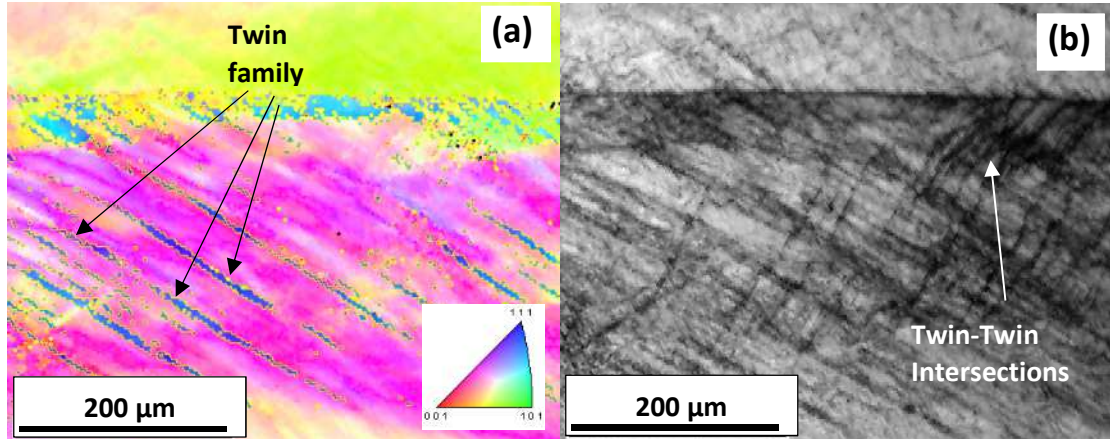
#### Post-test microstructures:

Figure 7 illustrates inverse pole figure (IPF) maps from EBSD of 40% rolled condition before and after SHPB compression. Nanoscale deformation twinning has been reported by Otto [11] in an FCC HEA of low SFE, CoCrFeMnNi during low temperature quasi-static tensile deformation. The lower stacking fault energy (SFE) of  $\text{Al}_{0.1}\text{CoCrFeNi}$  HEA appears to have increased its twinning propensity, causing deformation twinning even from the sub-dynamic process of deformation in a rolling mill. Much larger scale deformation twins whose length often exceeded 100  $\mu\text{m}$ , were in the cold rolled material, as seen from Figure 2(b) and the IPF image in Figure 7(a). Figures 7(b) and 7(c) show EBSD images of the same 40% rolled material after subjection to a further 10% strain in SHPB. Misorientation profile along the highlighted yellow line in Figure 7(c) shows numerous  $\Sigma_3$  boundaries with 60° misorientation. The proliferation in twinning activity is also clear from the spike in the number of boundaries with 60° misorientation, which represent twin fault planes, after SHPB as seen from a comparison of graphs in Figures 7(d) and 7(e).



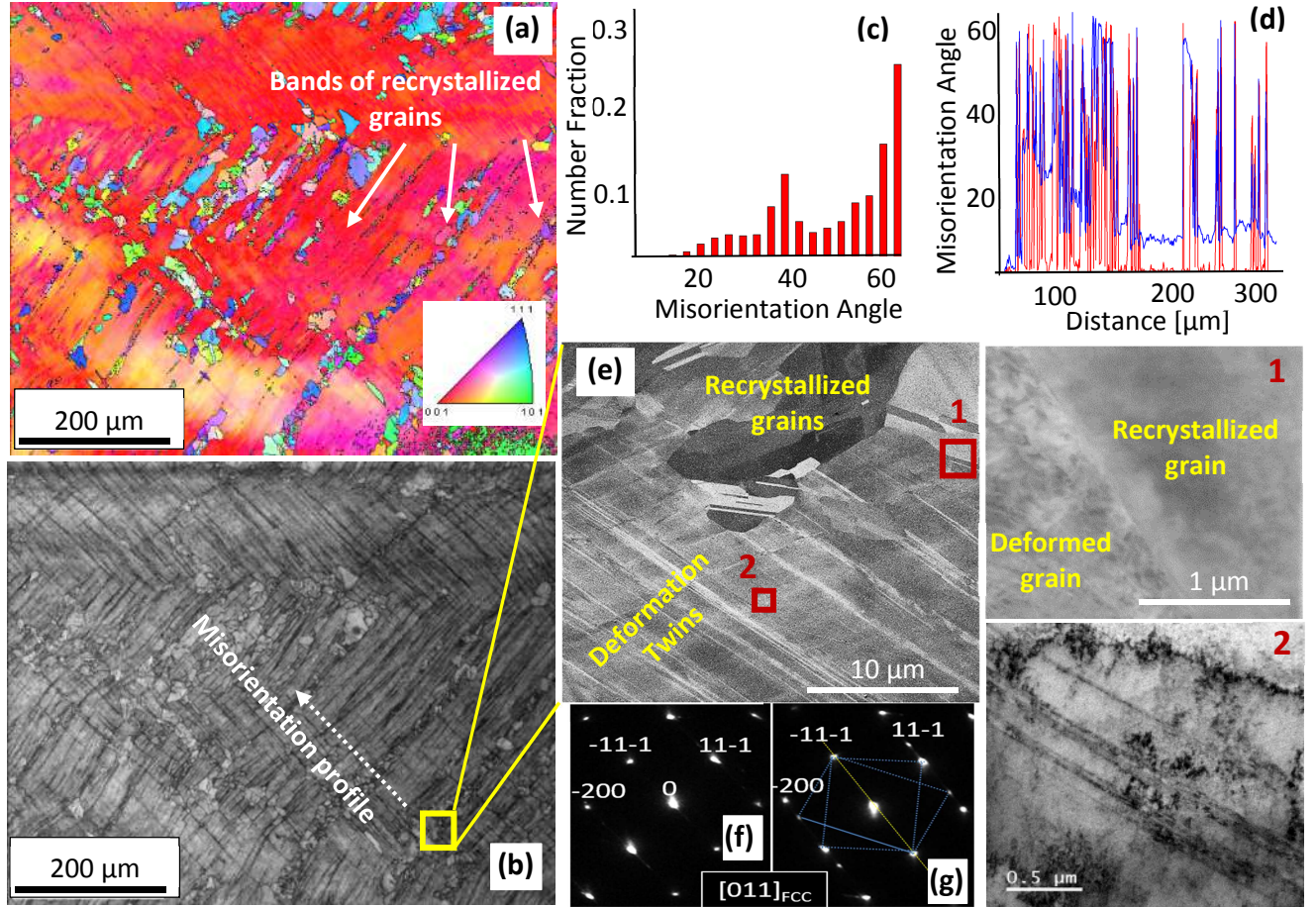
**Figure 7.** EBSD images of the 40% rolled material prior to and post SHPB compression. (a) IPF map before SHPB, (b) IPF map after SHPB, (c) IQ map before SHPB with misorientation profiling in inset (d) Number fraction of boundary misorientation before SHPB, and (e) after SHPB.

Figure 8 depicts microstructure of the low temperature annealed 550°C/24h condition after SHPB compression to ~10% strain showing multiple families of large deformation twins and their intersections (Figures 8 (a) and 8 (c)).



**Figure 8.** Microstructures of the recovery annealed 550°C/24h condition post SHPB deformation: (a) IPF map, and (b) IQ-IPF map from EBSD.

The post-SHPB microstructure of the other annealed condition, 620°C/50h, showed not only more extensive twinning but also evidence of shear localization, as seen from the EBSD and TEM images in Figure 9. IPF map from EBSD in Figure 9(a) shows parallelly aligned narrow strips of randomly oriented grains of very fine scale. IQ map of this region, Figure 9(b), shows extensive twinning in the surrounding regions. Evidence of extensive twinning is also observed by misorientation profiling in Figure 9(c), and the spike in the number fraction of boundaries with 60° misorientation in Figure 9(d). Figure 9(e) is a high resolution SEM image depicting a region of fine grains, and a large number of deformation twins outside these grains. Inset region2 shows STEM image of deformation twins in the sheared region, confirmed by the mirror spots in SADP pattern (Figure 9(g)) from the twin fault plane. As the prior condition was composed of only large grains with deformation bands and annealing twins, these small grains could have formed only during dynamic deformation. Further, the occurrence of fine grains in only narrow strips with heavily-bent, adjacent twins indicated they formed in regions of intense strain accumulation; i.e., shear localization. Dynamic recrystallization almost universally occurs in adiabatic shear bands due to rapid temperature rise [26] and can result in formation of fine grains. This theory is supported by the Bright-Field TEM from inset region1 showing the interior of such a newly formed grain appearing to be very clean compared to its neighboring deformed region, which has several defects and dislocation tangles within. The deformation bands seen in this annealed microstructure, Figure 3(b), could have aided in further strain localization during SHPB.



**Figure 9.** Microstructures of the recovery annealed 620°C/50h condition post SHPB deformation: (a) IPF map and (b) IQ map from EBSD, (c) Number fraction of boundary misorientation graph, (d) Misorientation profiling along dotted line in IQ map, (e) High resolution SEM with (Inset1) Bright-Field TEM comparing interiors of recrystallized and deformed grains (Inset2) STEM image showing deformation twins, (f) SADP pattern of the fcc grain (g) SADP pattern from twinned region.

The EBSD images of the recrystallized material after SHPB deformation are shown in Figure 10. Figures 10(a) and 10(b) show IPF and IQ-IPF images of 800°C/1h condition after a HSR compression to 10% strain. Figures 10(c) and 10(d) represent the microstructures after quasistatic tensile testing to 40% strain, showing extensive twinning in highly elongated grains. Misorientation profiling of this microstructure shows numerous 60°/Σ3 boundaries below. On the other hand, the post-SHPB microstructure from the recrystallized region showed neither a noticeable elongation of grains nor any deformation twins, but displayed highly heterogeneous strain distribution in some grains. These regions accommodating heavy strain did not index well in IPF mapping (Figure 10(a)) and appeared dark in IQ mapping (Figure 10(b)). This was not a manifestation of improper specimen preparation, because there were occasional annealing twins in the strained regions which indexed well, including distinct boundaries. Such areas are highlighted in Figure 9(a) by dark circles, confirm heterogeneous slip accommodation in only some grains during dynamic deformation. This could be due to suppression of twinning activity

in the smaller grains of the recrystallized region, as observed by Wu et al. [13]. There could still be deformation twinning in the prior-strained regions, which is very probable from the high dynamic work hardening of this condition.

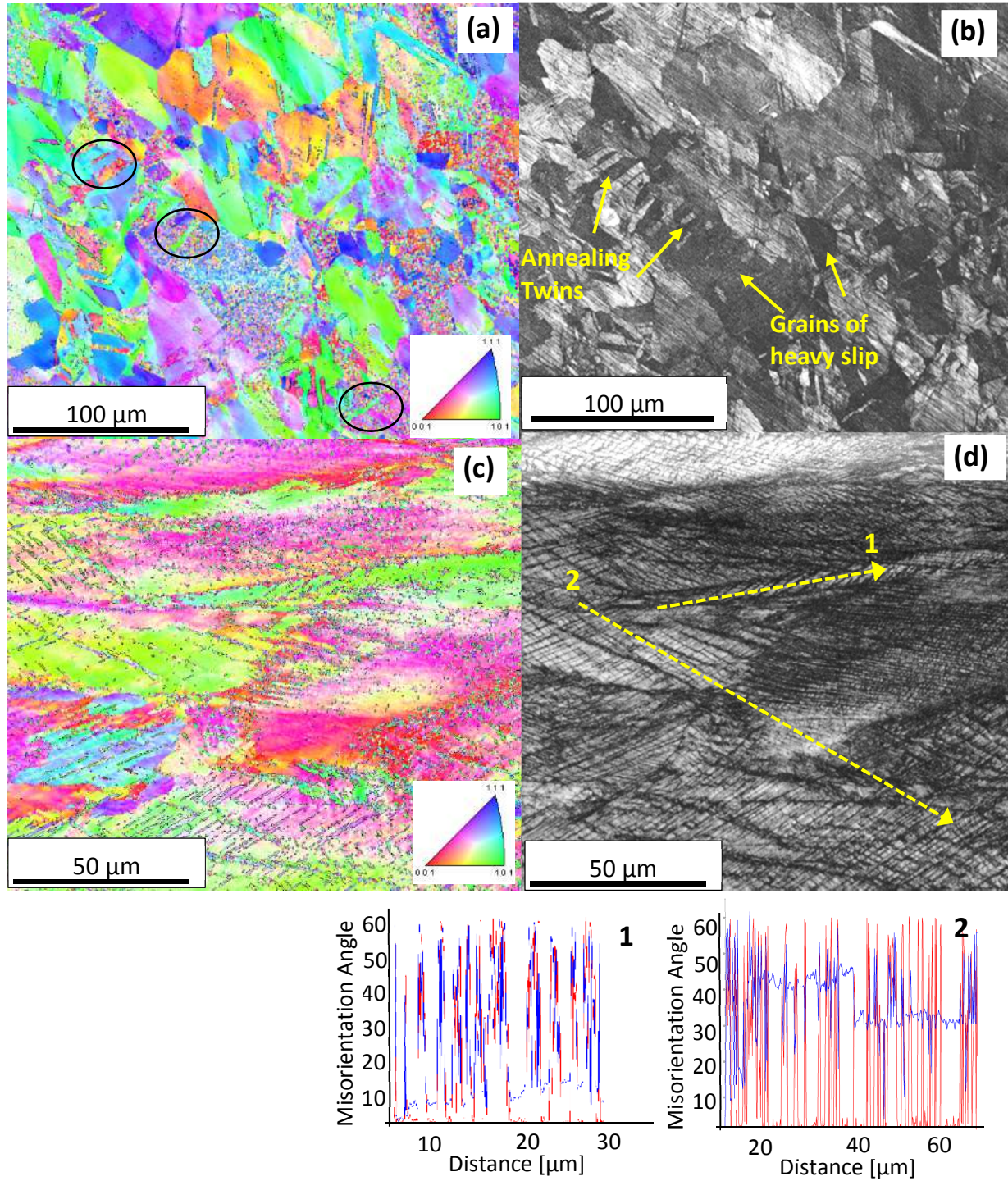


**Figure 10.** Microstructures of the 800 °C/1h specimen post deformation: (a) IPF and (b) IQ-IPF maps after SHPB compression (c) IPF and (d) IQ-IPF maps after quasistatic tension with misorientation profiles along the highlighted lines 1 and 2 below.

#### Discussion:

Comparison of the mechanical response of the cast and rolled materials in LSR and HSR regimes from Figure 5, showed the HSR regime's work hardening to be distinctly different from that of LSR. This contrast is highlighted in Figure 11, which compares work-hardening of the cast and 40% rolled conditions. The derivative [ $d\sigma/d\varepsilon = \theta$ ] is calculated from stress-strain curves of LSR and HSR of Figure 2.

In the cast-condition, the low strength of the material coupled with low SFE result in a steady work hardening rate at LSR (Figure 11 (a)), until sufficient stress level is attained for activation of screw dislocations for cross-slip [27]. After 800 MPa strength is attained at 60% strain, dynamic recovery appears triggered. Work hardening drops swiftly after this point, reaching zero at 62% strain, its necking point. In the 40% rolled material, where YS itself is very high, the flow stresses seem sufficient to trigger cross-slip right from the beginning. Here,  $\theta$  appears to be dropping steadily with strain (Figure 11(c)), reaching zero at the necking point, which is only 6%.

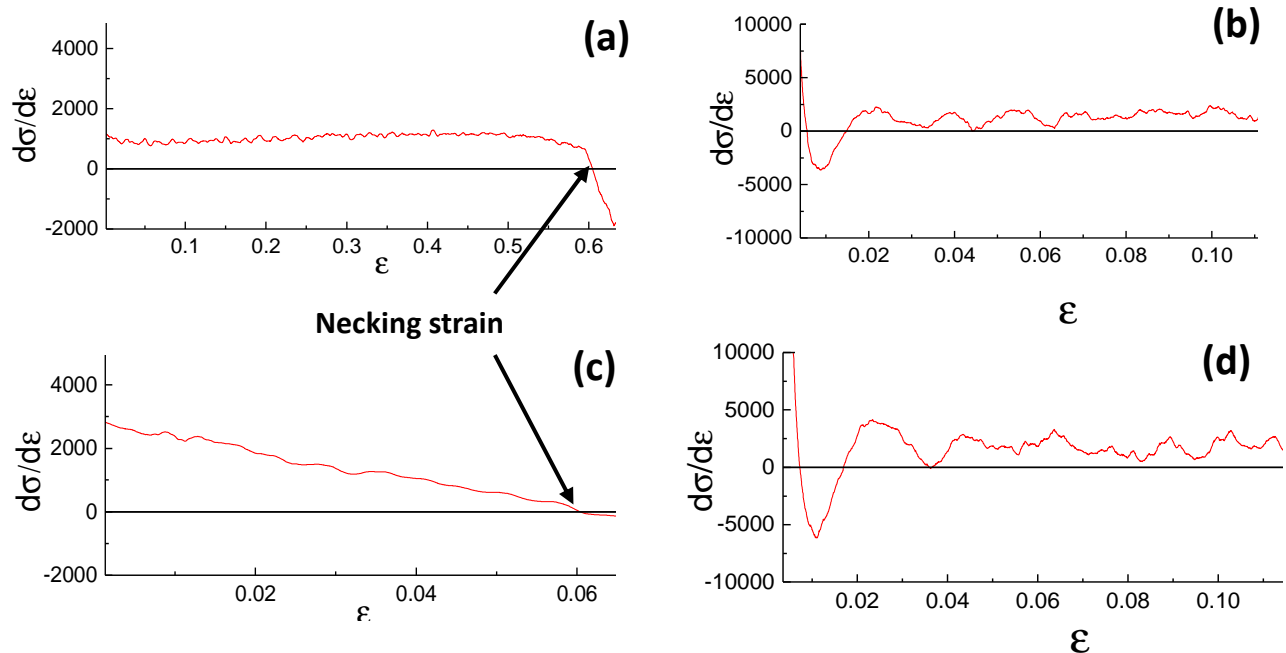


**Figure 11.** Comparison of the HSR and LSR work-hardening behaviors of the cast and 40% rolled conditions: (a)  $\theta_{LSR}$  - cast, (b)  $\theta_{HSR}$  - cast, (c)  $\theta_{LSR}$  - 40% rolled, and (d)  $\theta_{HSR}$  - 40% rolled.

Figures 11(b) and 11(d) show dynamic work hardening of the cast and the 40% rolled conditions. Here, data prior to 2-3% strain needs to be ignored, as the SHPB data is unreliable in the initial strains due to the time required for sufficient wave reverberations and strain rate

stabilization. Pohammer-Chree oscillations [21] in the SHPB data cause fluctuations in HSR work hardening, but in the physical sense it is representing only a stable value. At HSR,  $\Theta$  of both conditions remained steadily high until end of the test, at 1640 MPa in the cast condition and 1551 MPa in the rolled condition. The clear shift in the work hardening behavior from LSR to HSR regimes is attributed to suppression of dynamic recovery (DR) processes at high loading rates due to lack of sufficient time [12]. Total work hardening is given by:

$$\frac{d\sigma_p}{d\varepsilon} = \Theta = \Theta_0 \pm \Theta_r(\dot{\varepsilon}, T, \sigma_p, \varepsilon) \quad (1)$$

where  $\Theta_0$  is the athermal term, which in FCC metals is given by geometrical statistical dislocation storage rate and is purely an introduction of randomly distributed tangled dislocation networks. The second term,  $\Theta_r$ , is the rate of reorganization and annihilation of these dislocations. This process, and the resultant relaxation, is called dynamic recovery. At higher T or slower  $\dot{\varepsilon}$ , increase in  $\sigma$  or  $\varepsilon$  favors cross-slip and hence dynamic recovery and hence the drop in total work hardening. But in this case, we have contrast conditions of low SFE + high  $\dot{\varepsilon}$  + low T, which would inhibit dynamic recovery processes.

Evidence of suppression of dynamic recovery during high strain rate deformation is observed in the post-SHPB microstructures. Figure 13 shows STEM images of dislocation networks and loose dislocation tangles formation in the post-SHPB microstructure of 620°C/50h annealed condition. Due to insufficient time, there was no reorganization of dislocations into cells, but remain as loose tangles.

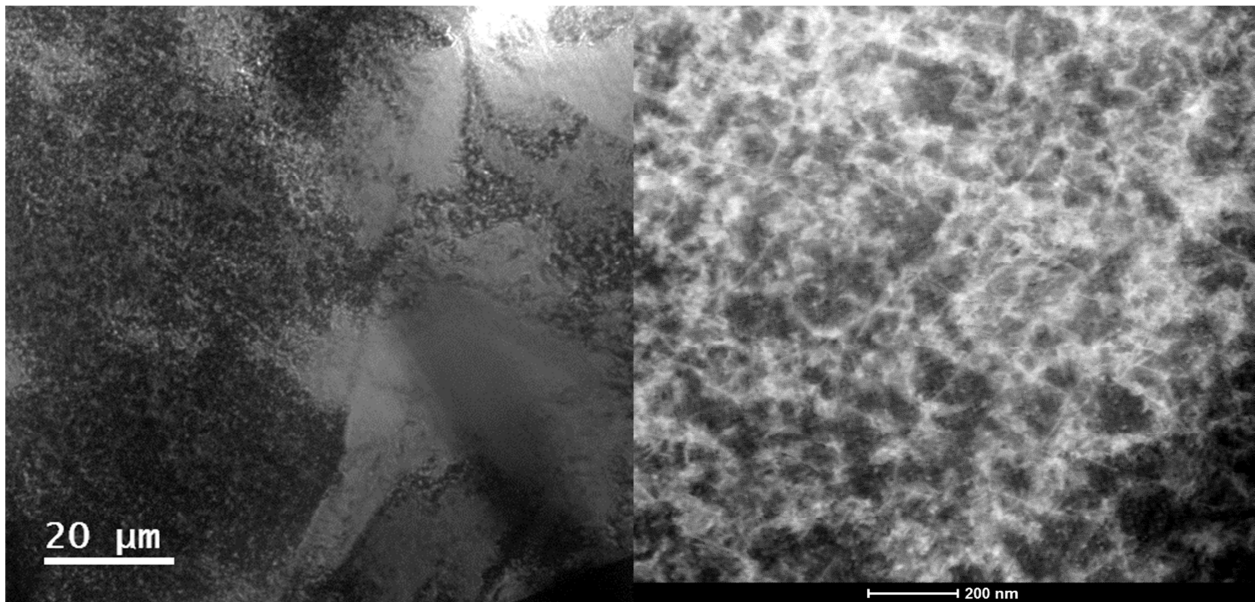


**Figure 12.** STEM images of microstructure of recovery annealed 620°C/50h condition post SHPB deformation (a) dislocation networks (b) higher magnification image showing dislocation cell formation.

In such an unrelaxed microstructure, the stress required for dislocation motion could also easily exceed twinning stress. In the case of HEAs, where twinning appeared to be a prominent mechanism, increased twinning activity at HSR is an additional contribution to work hardening, due to continual introduction of new obstacles in the form of twin boundary planes.

$$\frac{d\sigma_p}{d\varepsilon} = \Theta = \Theta_0 \pm \Theta_r(\dot{\varepsilon}, T, \sigma_p, \varepsilon) \pm \Theta_{Twin}(\dot{\varepsilon}, T, \sigma_p, \varepsilon) \quad (2)$$

Hence, a combination of dynamic recovery suppression and increased twinning activity are attributed as the cause of the observed high work hardening, > 1600 MPa, in this HEA.

The strain rate dependence of the cast condition is very similar that of a conventional FCC alloy [12]. It demonstrates both higher strength as well as higher work hardening at higher strain rates, as seen in Figure 5. However, this difference between HSR flow stresses and their LSR counterparts dropped with increasing cold work. This reducing gap indicates that strain rate sensitivity (SRS) decreases with cold work. To demonstrate this clearly, HSR and LSR stress-strain curves of each of the cast and rolled conditions are presented in Figure 13. Strain rate sensitivity,  $m$ , was calculated from HSR and LSR stress-strain curves for each of the microstructures as:

$$m = \left[ \frac{\partial \ln \sigma}{\partial \ln \dot{\varepsilon}} \right]_{T=RT, \varepsilon=0.02} \quad (3)$$

where  $\sigma$  is flow stress,  $\dot{\varepsilon}$  is strain rate,  $T$  is test temperature and  $\varepsilon$  is strain.

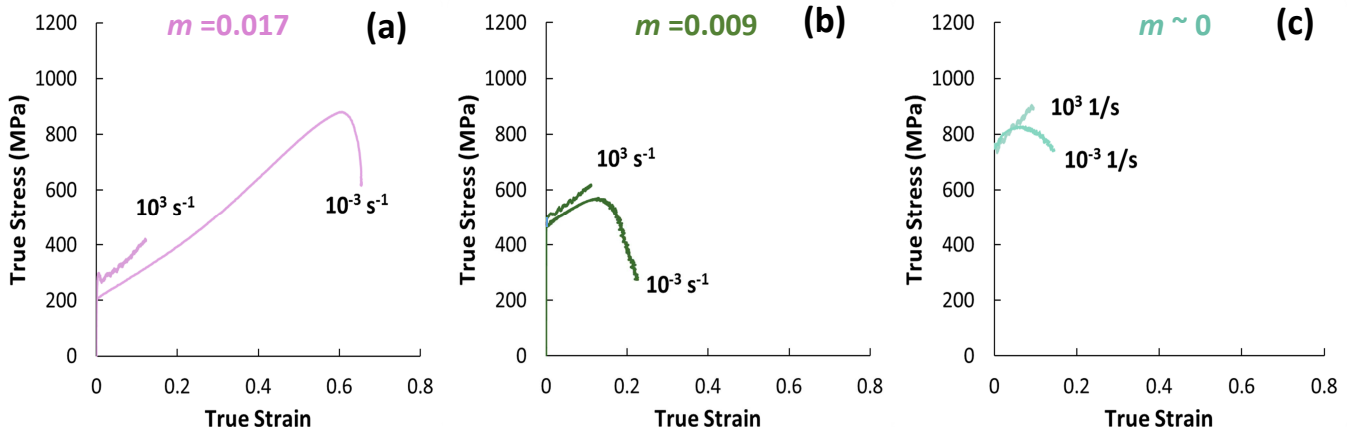


**Figure 13.** Comparison of strain rate dependence in the cast and rolled materials through HSR and LSR true stress-true strain curves. (a) Cast condition, (b) 20% cold-rolled condition, and (c) 40% cold-rolled condition. From left to right, SRS is observed to drop as the material is subjected to cold work further.

With slip as the preceding mechanism before twinning can occur, as given by Mahajan [28], the strain rate sensitivity arises from those contributions to strength that have a temperature

dependence. So from definition, strain rate sensitivity is microstructure-sensitive, as it depends on the type of obstacles to the motion of dislocations [29]. The amplitude of long-range obstacles is too large for thermal activation. These strength contributions are athermal and have no dependence on strain rate/temperature. Short range obstacles where thermal activation can help overcome these barriers bring strain rate dependence. MTS model [30] gives the total stress necessary for deformation can be given by a summation of athermal and thermal contributions:

$$\sigma = \sigma_{thermal} + \sigma_{athermal} \quad (4)$$

Hence SRS is determined by the relative contributions from these two types of strength components. In typical FCC metals, the internal stresses are considered insignificant. But for HEAs, large friction stress ( $\sigma_{FS}$ ) values were reported due to significant lattice distortion and varying dislocation mobility [31]. They are also reported to have large P-N barriers ( $\sigma_{P-N}$ ), as Wu et al observed from severe temperature dependence of tensile properties of CoCrFeMnNi HEA [32]. With multiple solute atoms, the HEAs also show strong solid solution strengthening ( $\sigma_{SS}$ ) [33]. While these three intrinsic contributions could escalate SRS, mechanical processing such as cold-rolling introduces dislocations ( $\sigma_{DIS}$ ), and deformation twins ( $\sigma_{TW}$ ) into structure. Similarly grain refinement during recrystallization introduces additional grain boundaries ( $\sigma_{GB}$ ). These are all long-range and athermal obstacles which mitigate SRS. So the total strength of this single phase HEA after a given processing condition is given by:

$$\sigma = (\sigma_{FS} + \sigma_{P-N} + \sigma_{SS})_{thermal} + (\sigma_{GB} + \sigma_{DIS} + \sigma_{TW})_{athermal} \quad (5)$$

With a high density of intrinsic defects, leading to higher dislocation-dislocation intersection, HEAs usually show high SRS. However, during the thermomechanical processing, the microstructures were heavily altered and the nature of obstacles to slip deformation also varied accordingly. The cast condition in the simplest form is composed of relatively defect-free, coarse grains. Here the main obstacles are short-range in nature, apart from a few long-range grain boundaries. The cast condition hence shows a modest SRS of 0.017. During cold working, this material is loaded with dislocations and deformation twins. These athermal stress contributions are significant as seen from the substantial rise in strength with cold work. YS increased by 265 MPa after 20% rolling, and 550 MPa after 40% rolling. As the athermal stress contributions dominate, SRS drops with cold work.

After the heat treating the rolled material, the nature of obstacles would be again altered as seen from the annealed microstructures in Figures 3 and 4. The LSR and HSR mechanical responses of the recovery annealed conditions are compared in Figure 14. With higher treatment temperature and longer duration, there is more recovery of the defects introduced by cold work, and as a result the 620°C/50h condition shows lower yield strength and higher work hardening. The dynamic work hardening of both conditions is comparable to that of the cast condition (1550 MPa slopes highlighted with dotted lines). SRS also recuperates from lowered athermal stress contribution, with reduction in dislocation and deformation twin

density. The  $550^{\circ}\text{C}/24\text{h}$  shows a well recuperated SRS of 0.017. The presence of deformation bands and small annealing twins within them appear to affect SRS of  $620^{\circ}\text{C}/50\text{h}$ , resulting in a slightly lower value of 0.014.

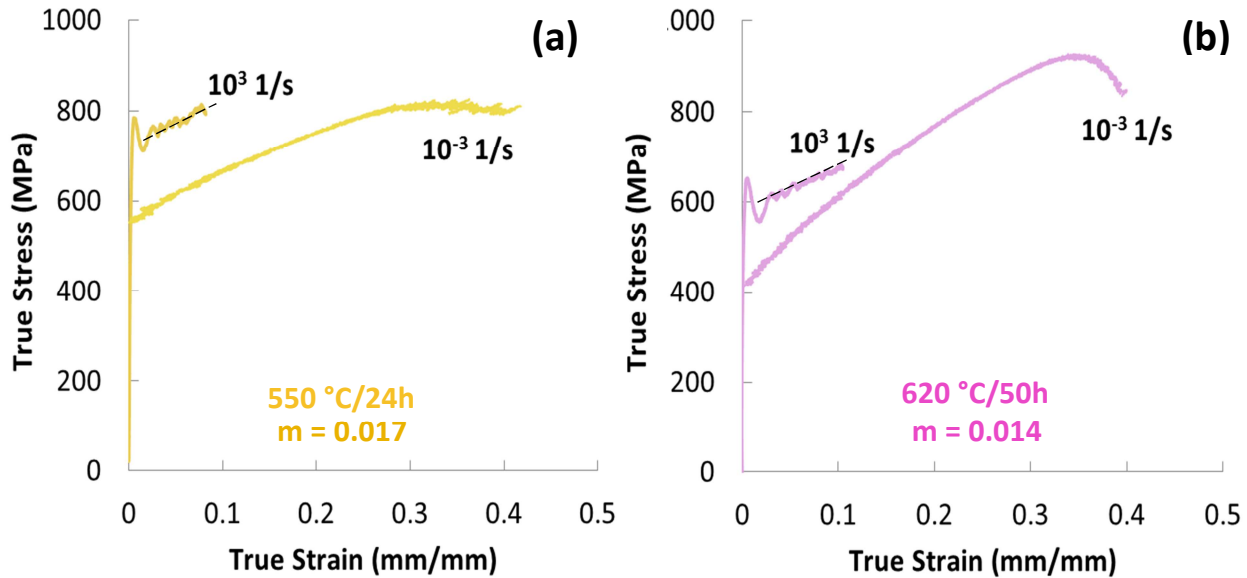


**Figure 14.** True stress-true strain curves from LSR ( $10^{-3} \text{ s}^{-1}$ ) and HSR ( $10^3 \text{ s}^{-1}$ ) regimes in (a)  $550^{\circ}\text{C}/24\text{h}$  and (b)  $620^{\circ}\text{C}/50\text{h}$  conditions.

The two recrystallization treatments' HSR and LSR mechanical response is illustrated in Figure 15. Even with the partial recrystallization, ductility of up to 30% was achieved, and both conditions show a work hardening of 1650 MPa in HSR. The  $700^{\circ}\text{C}/5\text{h}$  treatment, which resulted in smaller grains with remnant cold work, showed a higher YS of 505 MPa; whereas the  $800^{\circ}\text{C}/1\text{h}$  treatment with larger, equiaxed recrystallized grains showed a lower YS of 377 MPa.

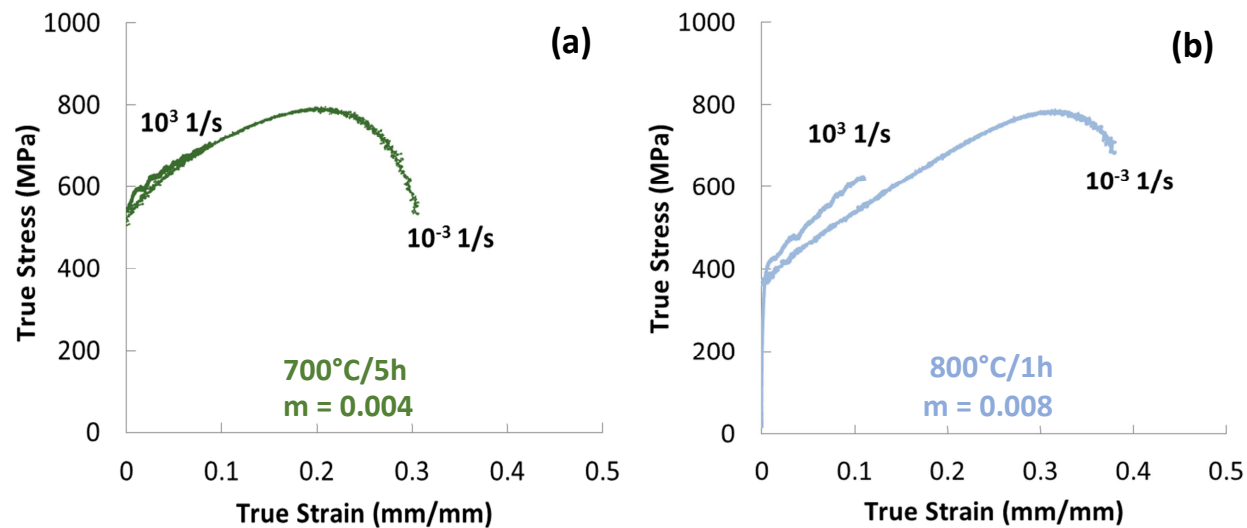


**Figure 15.** True stress-true strain curves from LSR ( $10^{-3}$  1/s) and HSR ( $10^3$  1/s) regimes in 700°C/5h and (e) 800°C/1h conditions.

The extent of SRS recuperation from recrystallization treatments is hence considerably smaller than that from recovery treatments. SRS in the 700°C/5h condition was very low,  $m = 0.004$ , while the 800°C/1h treatment resulted in slightly higher SRS, with  $m = 0.008$ . This is because, unlike recovery, recrystallization introduces a large numbers of fine grains whose boundaries act as long-range obstacles. So, if we assume that the strength gain in a generic partial recrystallized structure, compared to the cast condition, originates from a combination of grain refinement and some remnant cold work in the strained prior grains:

$$\sigma_{\text{partial reXn}} - \sigma_{\text{cast}} = X \beta \left[ \frac{1}{\sqrt{d}} - \frac{1}{\sqrt{D}} \right] + (1 - X)(\sigma_{\text{CR,r}}) \quad (6)$$

where  $X$  is the fraction of recrystallized regions and  $d$  is the recrystallized grain size,  $D$  is the original prior grain size,  $\sigma_{\text{CR,r}}$  is the remnant cold work after any recovery at high temperature.

In the 800°C/1h condition, YS gain is  $\sigma_{800\text{ °C}/1\text{h}} - \sigma_{\text{cast}} = 377-200 \text{ MPa} = 177 \text{ MPa}$ . The fraction of recrystallized regions here was calculated to be 0.38 from the low magnification SEM image in Figure 9 (b). EBSD map (Figure 9 (h)) showed the recrystallized grain size to be  $\sim 50 \mu\text{m}$ , while the prior grains were about  $500 \mu\text{m}$ . Komarasamy et al. [29] have calculated the Hall-Petch constant ( $\beta$ ) of this HEA to be  $371 \text{ MPa}\cdot\mu\text{m}^{0.5}$ . Therefore, the strength gain from grain refinement would be  $0.38 * 371 \left[ \frac{1}{\sqrt{50}} - \frac{1}{\sqrt{500}} \right] \text{ MPa} = 13 \text{ MPa}$ . That implies the remaining 164 MPa originates from the remnant cold work in the prior grains. The strength gain in the pure rolled material was  $\text{YS}_{800\text{ °C}/1\text{h}} - \text{YS}_{\text{cast}} = \sigma_{\text{CR}} = 750-200 \text{ MPa} = 550 \text{ MPa}$ . If the prior grains were completely unrecovered, their contribution should have been  $0.62 * 550 \text{ MPa} = 341 \text{ MPa}$ . Therefore, the extent of remnant cold work in the prior grains,  $\left[ \frac{\sigma_{\text{CR,r}}}{\sigma_{\text{CR}}} \right]$ , is  $\sim 48\%$ .

The strength gain in the 700°C/5h condition is higher,  $\sigma_{700\text{ °C}/5\text{h}} - \sigma_{\text{cast}} = 305 \text{ MPa}$ . The fraction of recrystallized regions estimated from low magnification SEM image in Figure 9(a) was 0.55. For this condition, the Hall-Petch strength addition would be larger as the recrystallized grain size is much smaller,  $5 \mu\text{m}$ , and  $X\beta \left[ \frac{1}{\sqrt{d}} - \frac{1}{\sqrt{D}} \right]$  here would be  $\sim 82 \text{ MPa}$ . However, cold work is still remnant in these regions to some extent. The prior grains would have higher extent of cold work. The remainder of the YS gain of 223 MPa must be from this remnant cold work, which can be calculated as above to be,  $\left[ \frac{\sigma_{\text{CR,r}}}{\sigma_{\text{CR}}} \right] \sim 90\%$ . The higher recrystallization fraction, the smaller grain size due to which large numbers of new grain boundaries are introduced, coupled with the high amount of remnant cold work, lead to a low SRS of  $m=0.004$ . So a combination of strength addition from grain refinement in the recrystallized region, and remnant cold work in the unrecrystallized regions, together leads to lower SRS recuperation in these conditions.

To summarize, strain rate sensitivity is highly microstructure-dependent in this single-phase FCC HEA. SRS of different microstructural conditions are summarized in Table1. A moderate SRS in

the cast condition originating from intrinsic obstacles, is lowered significantly with cold work, due to introduction of long range obstacle of dislocation tangles and deformation twins. Recovery annealing treatment on the cold worked material, which lowers defect density, recuperates SRS well. Higher temperature annealing, which resulted in partial recrystallization, showed a lower SRS < 0.008 due to high amounts of retained cold work in remnant prior grains and introduction of new grain boundaries in the recrystallized regions.

Table 1: Strain rate sensitivity of the various thermomechanically processed conditions.

Condition	Strain rate sensitivity $m = \left[ \frac{\partial \ln \sigma}{\partial \ln \dot{\epsilon}} \right]$
As-cast	0.017
20% CR	0.009
40% CR	0
40%CR+550°C/24h (Recovery)	0.017
40%CR+620°C/50h (Recovery)	0.014
40%CR+700°C/5h (Partial Recrystallization)	0.008
40%CR+800°C/1h (Partial Recrystallization)	0.004

## Conclusions

Strain rate sensitivity was highly microstructure-dependent in this single-phase FCC HEA Al<sub>0.1</sub>CoCrFeNi of low strength, moderate SRS, but high work-hardening potential. Significant strength improvements were achieved through cold-working the cast material without any loss in dynamic work hardening, but SRS dropped sharply due to introduction of new long-range barriers. Subsequent heat treatments are hence imperative to improve both ductility and SRS.

- Recovery: At 550°C, recovery was limited, but at 620°C, deformation twins were also recovered or transformed to annealing twins by boundary sweeping. Recovery of these long-range obstacles brought SRS back to cast condition levels and improved ductility to ~ 40%, while work-hardening was retained through intense twinning.
- Recrystallization: At 700°C, well-dispersed, 5µm-sized, fine grains formed in barely recovered remnant prior grains. Recrystallization was partial at 800°C as well, but due only to insufficient stored strain energy in some grains. A different kind of heterogeneous structure with pocketed regions of fully equi-axed, coarser, 50 µm-sized, recrystallized grains was formed. YS calculations indicated that cold work was partially recovered in the remnant prior grains here. Due to introduction of new grain boundaries in recrystallized regions and only partial recovery of cold work in the remnant grains, SRS was lower than recovered conditions, and ductility recuperated only up to 30%, while work hardening increased.

Hence, both these thermomechanical processing routes result in higher strength, recuperated SRS and ductilities, and retained work hardening levels.

## Acknowledgements

The work was performed under a cooperative agreement between the Army Research Laboratory and the University of North Texas (W911NF-16-2-0189). We also acknowledge the Materials Research Facility at UNT for microscopy facilities.

**Data Availability:**

The raw data and the processing required to reproduce these findings are available to download and will be uploaded along with the manuscript.

**References:**

1. Gao, M. C. "High-Entropy Alloys". Springer International Publishing, 2016.
2. Yeh, J.W. "Novel alloy concept, challenges and opportunities of high-entropy alloys." B. Raj (Ed.), *Frontiers Design Materials*, CRC Press (2007): 31-47.
3. Tsai, M-H. "High-entropy alloys: a critical review." *Materials Research Letters* 2.3 (2014): 107-123.
4. Zhang, Y. "Solid-solution phase formation rules for multi-component alloys." *Advanced Engineering Materials* 10.6 (2008): 534-538.
5. Wang, W.R. "Phases, microstructure and mechanical properties of  $\text{Al}_x\text{CoCrFeNi}$  high-entropy alloys at elevated temperatures." *Journal of Alloys and Compounds* 589 (2014): 143-152.
6. Wang, W.R. "Effects of Al addition on the microstructure and mechanical property of  $\text{Al}_x\text{CoCrFeNi}$  high-entropy alloys." *Intermetallics* 26 (2012): 44-51.
7. Joseph, J. "Understanding the mechanical behaviour and the large strength/ductility differences between FCC and BCC  $\text{Al}_x\text{CoCrFeNi}$  high entropy alloys." *Journal of Alloys and Compounds*, 726 (2017): 885-895.
8. Chou, H.P. "Microstructure, thermophysical and electrical properties in  $\text{Al}_x\text{CoCrFeNi}$  ( $0 \leq x \leq 2$ ) high-entropy alloys." *Materials Science and Engineering: B* 163.3 (2009): 184-189.
9. Komarasamy, M. "Serration behavior and negative strain rate sensitivity of  $\text{Al}_{0.1}\text{CoCrFeNi}$  high entropy alloy." *Intermetallics* 84 (2017): 20-24.
10. Kumar, N. "High strain-rate compressive deformation behavior of the  $\text{Al}_{0.1}\text{CrFeCoNi}$  high entropy alloy." *Materials & Design* 86 (2015): 598-602.
11. Otto, F. "The influences of temperature and microstructure on the tensile properties of a  $\text{CoCrFeMnNi}$  high-entropy alloy." *Acta Materialia* 61.15 (2013): 5743-5755.
12. Gray III, George T. "High-strain-rate deformation: mechanical behavior and deformation substructures induced." *Annual Review of Materials Research* 42 (2012): 285-303.
13. Wu, S. W. "Strong grain-size effect on deformation twinning of an  $\text{Al}_{0.1}\text{CoCrFeNi}$  high-entropy alloy." *Materials Research Letters* 5.4 (2017): 276-283.
14. Moon, J. "On the strain rate-dependent deformation mechanism of  $\text{CoCrFeMnNi}$  high-entropy alloy at liquid nitrogen temperature." *Materials Research Letters* 5.7 (2017): 472-477.

15. Wei, Q. "Effect of nanocrystalline and ultrafine grain sizes on the strain rate sensitivity and activation volume: fcc versus bcc metals." *Materials Science and Engineering: A* 381.1-2 (2004): 71-79.
16. National Research Council. Opportunities in protection materials science and technology for future army applications. National Academies Press, 2011.
17. Luo, B. "Strain rate and hydrostatic pressure effects on strength of iron." *Mechanics of Materials* 114 (2017): 142-146.
18. Shui-Sheng, Y. U. "The strain-rate effect of engineering materials and its unified model." *Latin American Journal of Solids and Structures* 10.4 (2013): 833-844.16.
19. Cao, Y. "The influence of temperatures and strain rates on the mechanical behavior of dual phase steel in different conditions." *Journal of Materials Research and Technology* 4.1 (2015): 68-74.
20. Wang, Y. M. "Strain hardening, strain rate sensitivity, and ductility of nanostructured metals." *Materials Science and Engineering: A* 375 (2004): 46-52.
21. Chen, W.W. "Split Hopkinson (Kolsky) bar: design, testing and applications". Springer Science & Business Media, 2010.
22. Xu, X. D. "Transmission electron microscopy characterization of dislocation structure in a face-centered cubic high-entropy alloy Al0. 1CoCrFeNi." *Acta Materialia* 144 (2018): 107-115.
23. Pouraliakbar, H. "Microanalysis of crystallographic characteristics and structural transformations in SPDed AlMnSi alloy by dual-straining." *Journal of Alloys and Compounds* 696 (2017): 1189-1198.
24. Pouraliakbar, H. "Constrained groove pressing and subsequent annealing of Al-Mn-Si alloy: microstructure evolutions, crystallographic transformations, mechanical properties, electrical conductivity and corrosion resistance." *Materials & Design* 124 (2017): 34-46.
25. Hou, J. "Strengthening in Al0.25CoCrFeNi high-entropy alloys by cold rolling." *Materials Science and Engineering: A* 707 (2017): 593-601.
26. Huang, K. "A review of dynamic recrystallization phenomena in metallic materials." *Materials & Design* 111 (2016): 548-574.
27. Najafizadeh, A. "Predicting the critical stress for initiation of dynamic recrystallization." *ISIJ international* 46.11 (2006): 1679-1684.
28. Mahajan, S. "Critique of mechanisms of formation of deformation, annealing and growth twins: Face-centered cubic metals and alloys." *Scripta Materialia* 68.2 (2013): 95-99.
29. Nemat-Nasser, S. "Physically-Based Single and Polycrystal Plasticity Models and their Experimental Verification." *IUTAM Symposium on Computational Mechanics of Solid Materials at Large Strains*. Springer, Dordrecht, 2003.
30. Cai, M.C. "A constitutive description of the strain rate and temperature effects on the mechanical behavior of materials." *Mechanics of materials* 42.8 (2010): 774-781.
31. Kumar, N. "Friction stir processing of a high entropy alloy Al 0.1 CoCrFeNi." *JOM* 67.5 (2015): 1007-1013.

32. Wu, Z. "Temperature dependence of the mechanical properties of equiatomic solid solution alloys with face-centered cubic crystal structures." *Acta Materialia* 81 (2014): 428-441.
33. Zhang, Y. "Alloy design and properties optimization of high-entropy alloys." *Jom* 64.7 (2012): 830-838.